INTERNATIONAL JOURNAL FOR NUMERICAL METHODS IN FLUIDS
Int. J. Numer. Meth. Fluids 2006; **52**:1135–1157
Published online 7 April 2006 in Wiley InterScience (www.interscience.wiley.com). DOI: 10.1002/fld.1222

An explicit algebraic Reynolds stress model in turbulence

M. M. Rahman*,† and T. Siikonen

Laboratory of Applied Thermodynamics, Helsinki University of Technology, Sähkömiehentie 4, FIN-02015 HUT, Finland

SUMMARY

A new algebraic Reynold stress model is constructed with recourse to the realizability constraints. Model coefficients are made a function of strain and vorticity invariants through calibration by reference to homogeneous shear flow data. The anisotropic production in near-wall regions is accounted for substantially by modifying the model constants $C_{\varepsilon(1,2)}$ and adding a secondary source term in the ε equation. Hence, it reduces the kinetic energy and length scale magnitudes to improve prediction of adverse pressure gradient flows, involving flow separation and reattachment. To facilitate the evaluation of the turbulence model, some extensively used benchmark cases in the turbulence modelling are convoked. The comparisons demonstrate that the new model maintains qualitatively good agreement with the direct numerical simulation (DNS) and experimental data. Copyright © 2006 John Wiley & Sons, Ltd.

KEY WORDS: turbulence anisotropy; realizability; production to dissipation ratio; flow separation and reattachment

1. INTRODUCTION

With relevance to constantly increasing demands on predictive capability of the Reynolds-averaged Navier–Stokes (RANS) formulation for complex flows, the need for more appropriate turbulence closures has also escalated. Conceptually, the full Reynolds stress closure approach entangles the history/nonlocal effects of turbulence automatically and offers the most accurate predictive performance in calculating all types of turbulent flows. However, the Reynolds stress closure method inherits severe complications that discourage many users simply to implement it, particularly for complex flows where the integration up to the wall via a low-Reynolds number scheme is extremely important.

In principle, the Reynolds stress model is formulated to describe complex turbulent flows where there are significant departures from equilibrium. With the help of the equilibrium

*Correspondence to: M. M. Rahman, Laboratory of Applied Thermodynamics, Helsinki University of Technology, Sähkömiehentie 4, FIN-02015 HUT, Finland.
†E-mail: mizanur.rahman@hut.fi

Received 17 November 2005
Revised 6 February 2006
Accepted 16 February 2006

hypothesis, Rodi [1] proposed an idea of obtaining the algebraic stress model (ASM) from the second-order closure. Physically, two assumptions are made in the algebraic Reynolds stress closures: the difference between the convection and diffusion terms in the Reynolds stress equation is proportional to the corresponding difference in the turbulent kinetic energy equation, and the Reynolds stress anisotropy b_{ij} is constant along a streamline. It provides algebraic equations without solving the differential equations for the Reynolds stresses. Invoking the same equilibrium hypothesis as Rodi, Pope [2] developed a methodology to procure an explicit relation for the Reynolds stress tensor from the implicit algebraic stress model by using a tensorial polynomial expansion in the integrity basis. Gatski and Speziale [3] used this method to derive an explicit algebraic stress equation for two- and three-dimensional turbulent flows. In order to generalize the results, the algebraic stress representation is applied to the general class of pressure–strain correlation models [4], which are linear in the anisotropic tensor. After regularization, an anisotropic eddy viscosity model with strain-dependent coefficients is achieved, which has been referred to as an explicit ASM. The explicit model extends the ability of the two-equation models to account for nonequilibrium and anisotropic effects. However, the model shows evidence of numerical instability when the flow is far from equilibrium [5]. The reason is that the ASM is more susceptible to the rotational strains. Girimaji [6] developed a fully explicit, self-consistent variant of the Gatski–Speziale model, by solving the cubic equation for P_k/ε (production to dissipation ratio) arising in the context of the selected pressure–strain model. Although this achievement yielded a new model variant, the resulting solution for P_k/ε is unfortunately too cumbersome to be implemented.

At the two-equation level of turbulence modelling, the ASM unambiguously constitutes an attractive and viable alternative for the Reynolds stress model. However, the ASM is derived by subjecting the anisotropy transport equation to the weak equilibrium constraint that limits its application for flows where advection by the mean flow and turbulent transport dominate the evolution of the Reynolds stress [7]. In addition, the ASM contains the main weakness of the standard Reynolds stress closure model stemming from inadequate modelling of the pressure–strain correlation [8]. Despite these limitations, the ASM is viewed as one of the most sophisticated closure strategies and quite appropriate to capture the essential phenomenological features of turbulence. For instance, it retains a factor of major physical relevance, namely the distinction between the components of the Reynolds stress tensor, though not accounting for their transport histories.

The turbulence model developed in this study is an explicit ASM, constructed with resorting to the realizability constraints, i.e. the positivity of the normal Reynolds stresses and Schwarz' inequality between turbulent velocity correlations. Sticking to the realizability constraints, the model coefficients are made a function of strain and vorticity invariants through calibration by reference to DNS data for homogeneous shear flows. In near-wall regions, the anisotropic production in the ε equation is accounted for substantially by modifying the model constants $C_{\varepsilon(1,2)}$ and adding a secondary source term. The wall singularity is removed by using a physically appropriate time scale that never falls below the Kolmogorov time scale $\sqrt{\nu/\varepsilon}$, representing the time scale realizability enforcement accompanied by the near-wall turbulent phenomena. A near-wall eddy viscosity damping function f_μ is introduced which reproduces the distinct effects of low-Reynolds number and wall proximity. In addition, the turbulent Prandtl numbers $\sigma_{(k,\varepsilon)}$ are adjusted so as to provide substantial turbulent diffusion in near-wall regions.

The model performance is validated against experimental and DNS data of well-documented flows, consisting of a fully developed channel flow, a flat plate boundary layer flow with zero pressure gradient, a backward-facing step flow and an asymmetric plane diffuser flow, respectively. Particular attention is paid to assess the capability of the new model, relative to the low-Reynolds number linear k–ε models of So *et al.* [9] and Rahman and Siikonen [10], when used to predict the flows associated with transition, flow separation and reattachment. A concrete analysis of the simulated results is provided.

2. TURBULENCE MODELLING

The two-dimensional RANS equations, including the equations for the turbulent kinetic energy k and dissipation ε, can be written in the following form:

$$\frac{\partial U}{\partial t} + \frac{\partial (F - F_v)}{\partial x} + \frac{\partial (G - G_v)}{\partial y} = Q \tag{1}$$

where $U = (\rho, \rho u, \rho v, E, \rho k, \rho \varepsilon)^{\mathrm{T}}$. The inviscid fluxes are

$$F = \begin{pmatrix} \rho u \\ \rho u^2 + p + \frac{2}{3}\rho k \\ \rho uv \\ u(E + p + \frac{2}{3}\rho k) \\ \rho uk \\ \rho u\varepsilon \end{pmatrix}, \quad G = \begin{pmatrix} \rho v \\ \rho vu \\ \rho v^2 + p + \frac{2}{3}\rho k \\ v(E + p + \frac{2}{3}\rho k) \\ \rho vk \\ \rho v\varepsilon \end{pmatrix} \tag{2}$$

Here ρ is the density and p is the pressure. The total internal energy is defined as

$$E = \rho e + \frac{\rho \mathbf{V} \cdot \mathbf{V}}{2} + \rho k \tag{3}$$

where e is the specific internal energy and $\mathbf{V} = u\mathbf{i} + v\mathbf{j}$ is the velocity. The viscous fluxes are

$$F_v = \begin{pmatrix} 0 \\ \tau_{xx} + \frac{2}{3}\rho k \\ \tau_{xy} \\ u\tau_{xx} + v\tau_{xy} - q_x \\ \mu_k(\partial k/\partial x) \\ \mu_\varepsilon(\partial \varepsilon/\partial x) \end{pmatrix}, \quad G_v = \begin{pmatrix} 0 \\ \tau_{xy} \\ \tau_{yy} + \frac{2}{3}\rho k \\ u\tau_{xy} + v\tau_{yy} - q_y \\ \mu_k(\partial k/\partial y) \\ \mu_\varepsilon(\partial \varepsilon/\partial y) \end{pmatrix} \tag{4}$$

and the viscous stress tensor can be given as

$$\tau_{ij} = 2\mu(S_{ij} - \tfrac{1}{3}S_{kk}\delta_{ij}) - \rho\overline{u_i u_j} \tag{5}$$

where μ is the laminar viscosity, S_{ij} is the mean strain rate tensor and $\rho\overline{u_i u_j}$ are the Reynolds stresses. The heat flux is calculated from

$$\mathbf{q} = -\left(\mu\frac{c_p}{Pr} + \mu_T\frac{c_p}{\sigma_t}\right)\nabla T \tag{6}$$

where μ_T is the coefficient of turbulent eddy viscosity, c_p is the specific heat at constant pressure, Pr and σ_t represent the laminar and turbulent Prandtl numbers, respectively, and T implies the temperature. Clearly, the turbulent part of the total heat flux is estimated using the Boussinesq approximation. The value of σ_t is chosen to be 0.9 [11]. The diffusion of turbulence is modelled as

$$\mu_k\nabla k = \left(\mu + \frac{\mu_T}{\sigma_k}\right)\nabla k, \quad \mu_\varepsilon\nabla\varepsilon = \left(\mu + \frac{\mu_T}{\sigma_\varepsilon}\right)\nabla\varepsilon \tag{7}$$

where σ_k and σ_ε are the appropriate turbulent Prandtl numbers. The source term Q for the k and ε equations can be written as

$$Q = \begin{pmatrix} \rho P - \rho\varepsilon \\ \dfrac{C_{\varepsilon 1}\rho P - C_{\varepsilon 2}\rho\varepsilon + E_\varepsilon}{T_t} \end{pmatrix} \tag{8}$$

where the turbulent production term $P = -\overline{u_i u_j}(\partial u_i/\partial x_j)$ and E_ε is a secondary source term designed to increase the level of ε in nonequilibrium flow regions. The symbolized T_t is the characteristic (mixed/hybrid) time scale, having the asymptotic consistency in the near-wall region. The modelling of $\rho\overline{u_i u_j}$ in the explicit ASM and associated relevant aspects are discussed in some detail in subsequent sections.

2.1. Explicit ASM

The rationale provoking the extension of the Reynolds stress to nonlinear form refers to improved performance with the inclusion of strain rate and vorticity tensors to capture anisotropy. The explicit expansion to the Reynolds stress tensor $\rho\overline{u_i u_j}$ that constitutes an anisotropic eddy viscosity model can be written as [12]

$$\begin{aligned}\rho\overline{u_i u_j} = {} & \tfrac{2}{3}\rho k\delta_{ij} - 2\mu_T[(S_{ij} - \tfrac{1}{3}S_{kk}\delta_{ij}) + \alpha_1 T_t(S_{ik}W_{kj} + S_{jk}W_{ki}) \\ & - \alpha_2 T_t(S_{ik}S_{kj} - \tfrac{1}{3}S_{kl}S_{kl}\delta_{ij})]\end{aligned} \tag{9}$$

In particular, many quadratic stress–strain relations have been proposed to extend the applicability of linear eddy viscosity models at modest computational cost. However, comparison shows that none achieves much greater width of applicability for practical flows [13]. Therefore, one can certainly formulate more accurate alternative practices, for instance a cubic stress–strain relation, which is beyond the scope of the present work. Considering the quadratic approach as an example, this study is devoted to the removal of unphysical behaviour (i.e. negative energy components) from the model formulation, which is not guaranteed by many other nonlinear turbulence models [14].

Since the viscous dissipation presumably dominates near the wall, the eddy viscosity is evaluated from

$$\mu_T = C_\mu f_\mu \rho k T_t \tag{10}$$

where the dynamic time scale k/ε is replaced by T_t, a distinct turbulence time scale and f_μ denotes the eddy viscosity damping function. The model coefficients $(C\mu, \alpha_1, \alpha_2)$ in Equations (9) and (10) are in general scalar functions of the invariants formed on the strain rate S_{ij} and vorticity W_{ij} tensors in question [2, 3]:

$$S_{ij} = \frac{1}{2}\left(\frac{\partial u_i}{\partial x_j} + \frac{\partial u_j}{\partial x_i}\right), \quad W_{ij} = \frac{1}{2}\left(\frac{\partial u_i}{\partial x_j} - \frac{\partial u_j}{\partial x_i}\right) \tag{11}$$

The invariants of mean strain rate and vorticity tensors are defined by $S = \sqrt{2S_{ij}S_{ij}}$ and $W = \sqrt{2W_{ij}W_{ij}}$, respectively. The detailed functional forms of the model coefficients are determined relying on the constraints such as realizability and appropriate experiments.

The physically necessary conditions for a turbulence model are the realizability conditions that can be defined as [4]

$$\overline{u_i^2} \geqslant 0, \quad \frac{\overline{u_i u_j}^2}{\overline{u_i^2}\,\overline{u_j^2}} \leqslant 1 \tag{12}$$

Equation (12) also represents the minimal requirement to prevent a turbulence model from producing nonphysical results. The commonly used isotropic k–ε eddy viscosity model with a constant $C_\mu = 0.09$ becomes unrealizable in the case of a large mean strain rate parameter $T_t S$ (when $T_t S > 3.7$), producing negative normal stresses and Equation (12) is violated [15]. To ensure realizability, the model coefficient C_μ cannot be a constant. It must be related with the mean flow deformation rate.

Obviously, the anisotropic eddy viscosity model augments the capacity of the two-equation models to account for nonequilibrium effects through the coefficient C_μ. To serve this purpose, a plausible formulation for C_μ is devised as

$$C_\mu = \frac{1}{2(1 + T_t\sqrt{S^2 + W^2})} \tag{13}$$

Actually, C_μ is calibrated focusing attention on the homogeneous shear flow, characterized by

$$S_{12} = S/2 = S_{21}, \quad W_{12} = S/2 = -W_{21} \tag{14}$$

Based on this flow characteristic and the property $\lim_{S\to\infty} P_k/\varepsilon \sim S$ [16], an evolution equation for P_k/ε can be procured:

$$\frac{P_k}{\varepsilon} = C_\mu \eta^2 \tag{15}$$

where $\eta = T_t \max(S, W)$. It is appropriate to emphasize herein that the proposed relation meets the requirements of the equilibrium state: $P_k/\varepsilon \approx 1$ with $C_\mu \approx 0.09$ for the logarithmic region in a turbulent channel flow at $\eta = T_t(S = W) \approx 3.3$ [17], and $P_k/\varepsilon \approx 1.9$ with $C_\mu \approx 0.052$ for the homogeneous shear flow of Tavoularis and Corrsin [18] at $\eta = 6.0$, respectively. Note that

the log-layer of a channel flow is a region where the Reynolds stress equation has the same form as in the homogeneous case [19].

Figure 1 illustrates the distribution of C_μ as a function of $\eta = T_t(S = W)$. As is evident, the C_μ distribution is in excellent agreement with various DNS data [20–22]. The proposed C_μ is reduced significantly with increasing η and maintained at a level that could mimic the complex turbulent flows. However, it seems likely that C_μ converges toward a high value 0.5 (here, in particular, compared with the traditional $C_\mu = 0.09$) as $\eta \to 0$. In principle, the value of C_μ is very flow dependent and experimental evidences [23] indicate a range as large as 0.03–0.6, substantiating the behaviour of present C_μ worthily. The profiles of P_k/ε are displayed in Figure 2. Clearly, relation (15) recovers the self-consistent models of Girimaji [6] and Jongen

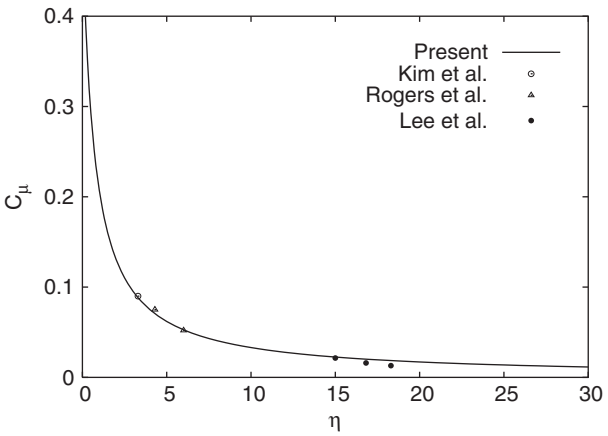

Figure 1. Distribution of C_μ as a function of shear parameter η.

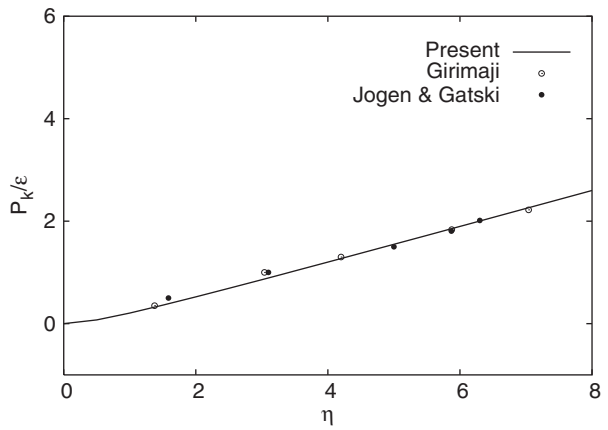

Figure 2. Locus of solution points for state variable P_k/ε as a function of η.

and Gatski [16] for the weak equilibrium condition. The new calibrated relation for P_k/ε can assist in determining the coefficients $\alpha_{(1,2)}$ in Equation (9).

To make the eddy viscosity model realizable, the necessity to account for changes in the coefficients $\alpha_{(1,2)}$ associated with Equation (9), is acknowledgeable. The constant coefficients $\alpha_{(1,2)}$ can potentially lead to the prediction of nonphysical normal stress components, and thereby violate the realizability principle. Recourse to the modelling relevancy (i.e. realizability constraints) and DNS data for homogeneous shear flows, the coefficients $\alpha_{(1,2)}$ are regularized as

$$\alpha_1 = \left(1 + \beta + 2\frac{P_k}{\varepsilon}\right)^{-1}, \quad \alpha_2 = \left(2 + \beta + 2\frac{P_k}{\varepsilon}\right)^{-1} \tag{16}$$

where $\beta = \sqrt{C_\mu P_k/\varepsilon}$ and P_k/ε is defined in Equation (15). Conspicuously, the coefficients are capable of responding to the shear/vorticity dominated flows and maintain the physical consistency in the context of a mild departure from equilibrium.

The Reynolds stress anisotropy, defined as

$$b_{ij} = \frac{\overline{u_i u_j}}{2k} - \frac{1}{3}\delta_{ij} \tag{17}$$

in homogeneous shear flow, can be derived from Equation (9) as

$$\begin{aligned} b_{11} &= \left(\frac{\alpha_1}{2} + \frac{\alpha_2}{12}\right)\frac{P_k}{\varepsilon}, \quad b_{22} = -\left(\frac{\alpha_1}{2} - \frac{\alpha_2}{12}\right)\frac{P_k}{\varepsilon} \\ b_{33} &= -(b_{11} + b_{22}) = -\frac{\alpha_2}{6}\frac{P_k}{\varepsilon}, \quad b_{12} = -\frac{1}{2\eta}\frac{P_k}{\varepsilon} \end{aligned} \tag{18}$$

Detailed comparisons of the anisotropies with the DNS data are shown in Table I for the channel flow of Reference [17] in the inertial sublayer at $\eta = 3.3$, and in Table II for the homogeneous shear flow of Tavoularis and Corrsin [18] at $\eta = 6.0$, respectively. Clearly, the

Table I. Anisotropy in the log layer of channel flow.

b_{ij}	DNS	Standard	Present
b_{11}	0.175	0.0	0.169
b_{12}	−0.145	−0.149	−0.145
b_{22}	−0.145	0.0	−0.131
b_{33}	−0.03	0.0	−0.038

Table II. Anisotropy in homogeneous shear flow.

b_{ij}	DNS	Standard	Present
b_{11}	0.202	0.0	0.212
b_{12}	−0.142	−0.273	−0.158
b_{22}	−0.145	0.0	−0.160
b_{33}	−0.057	0.0	−0.052

present model provides some anisotropy of Reynolds stresses for both the boundary layer and homogeneous shear flows, compared with the standard k–ε eddy viscosity model. Therefore, it is capable of predicting the turbulent driven secondary flows. The proposed model anisotropy is in fairly good agreement with the data. This improvement is mainly creditable to the behaviour of C_μ, persuading a nonequilibrium effect on the turbulent eddy viscosity.

The Lumley triangle, i.e. the anisotropy invariant map [4] contains all physically realizable states of turbulence. Every realizable Reynolds stress adhering to a turbulent flow corresponds to a point in the Lumley triangle. Figure 3 shows the behaviour of the present model in the $(\mathrm{III}_b, \mathrm{II}_b)$ phase space (where $\mathrm{II}_b = b_{ip}b_{pi}$ and $\mathrm{III}_b = b_{ip}b_{pq}b_{qi}$) for a wide range of shear parameters. As expected from the comparison with the DNS results (Tables I and II), the model yields predictions in close proximity to the invariant values from the DNS as well. Values of $\eta = T_t(S = W)$ in the range 0–200 are considered to be adequate to conduct the experiment. It is found that $\eta > 100$ induces small changes in the invariants and ultimately, the model saturates within the invariant triangle. This occurrence implies that even in a state with high shear rates, the anisotropy state is not forced out of the allowed region of the invariant map. Therefore, the present model ensures realizability for a pure shear flow.

The model realizability is further contrasted with the accelerated flow where turbulence can be strongly attenuated [14]. The turbulence attenuation is characterized by plane straining (where $W_{ij} = 0$ for all i and j), traditionally called stretching, rather than shear. Herein, the most pronounced attenuation of turbulence kinetic energy is the evolution of the component $\overline{u_1 u_1}$ in the direction of a primary strain S_{11}. The fundamental stretching field together with the continuity equation for incompressible flow suggests that the limiting states are [14]: the 2-D stretching

$$S_{22} = -S_{11}(S_{33} = 0), \quad S_{11} = S/2 \tag{19}$$

and the axisymmetric stretching

$$S_{22} = S_{33} = -S_{11}/2, \quad S_{11} = S/\sqrt{3} \tag{20}$$

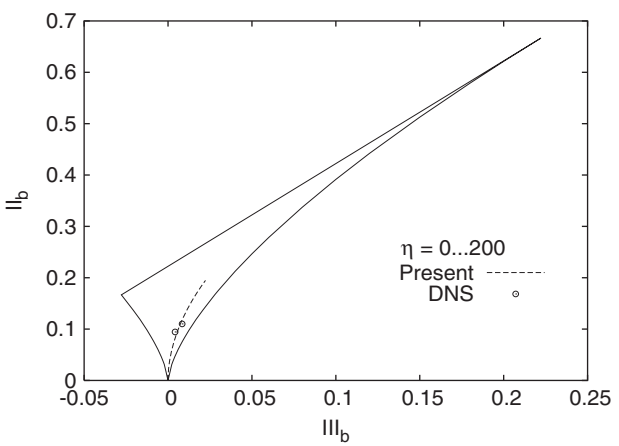

Figure 3. Homogeneous shear phase plane mapping at different shear rates.

The two cases in question are often associated with irrotational plane strain and axisymmetric contraction of the flow, having different implications on the model realizability. In both cases, the realizability principle applied to the present model implies that

$$\frac{\overline{u_1 u_1}}{2k} = \frac{1}{3} - C_\mu T_t \left[S_{11} - \alpha_2 T_t \left(S_{11} S_{11} - \frac{1}{3} S_{kk}^2 \right) \right] \geqslant 0 \tag{21}$$

The 2-D plane strain situation pertaining to Equation (21) may be given as

$$\frac{\beta}{2} \left(1 - \frac{\alpha_2}{6} \eta \right) \leqslant \frac{1}{3} \tag{22}$$

The corresponding axisymmetric contraction results in

$$\beta \left(\frac{1}{\sqrt{3}} - \frac{\alpha_2}{6} \eta \right) \leqslant \frac{1}{3} \tag{23}$$

where $\eta = T_t S$ and $\beta = \sqrt{C_\mu P_k / \varepsilon} = C_\mu \eta$ resembles the anisotropy of turbulence. With attention restricted to this flow situation, the model coefficients can be recast as

$$\begin{aligned} C_\mu &= \frac{1}{2(1+\eta)}, \quad \frac{P_k}{\varepsilon} = \frac{\eta^2}{2(1+\eta)} \\ \beta &= \frac{\eta}{2(1+\eta)}, \quad \alpha_2 = \left[2 + \frac{\eta(1+2\eta)}{2(1+\eta)} \right]^{-1} \end{aligned} \tag{24}$$

It can be easily verified that with Equation (24), relations (22) and (23) are satisfied at a moderate strain rate. However, if $\eta \gg 1$, then $\eta/(1+\eta) \approx 1$. In this case, the coefficients β and α_2 assume the following values:

$$\beta \approx \frac{1}{2}, \quad \alpha_2 \approx \frac{2}{5+2\eta} \tag{25}$$

Consequently, Equations (22) and (23) reduce to

$$\frac{1}{4} \left[1 - \frac{\eta}{3(5+2\eta)} \right] \leqslant \frac{1}{3}, \quad \frac{1}{2} \left[\frac{1}{\sqrt{3}} - \frac{\eta}{3(5+2\eta)} \right] \leqslant \frac{1}{3} \tag{26}$$

Subsequently, one can certainly derive the conclusion that for $\eta \gg 1$, inequality (26) is satisfied. Both states are placed in the Lumley triangle as shown in Figure 4. Evidently, each state remains in the allowed region of the invariant map. To this end, it must be stressed that the present model does not exhibit unrealizable features at moderate/severe strain rates.

2.2. *Near-wall modelling*

In the vicinity of the wall, the molecular viscosity effect is superior to the turbulence mixing, reflecting a strong anisotropic condition. Consequently, an important criterion regarding the appropriateness of the turbulence model is to represent the near-wall behaviour of turbulence quantities accompanied by a preferential damping of velocity fluctuations in the direction normal to the wall that reconciles the influence of wall proximity adequately.

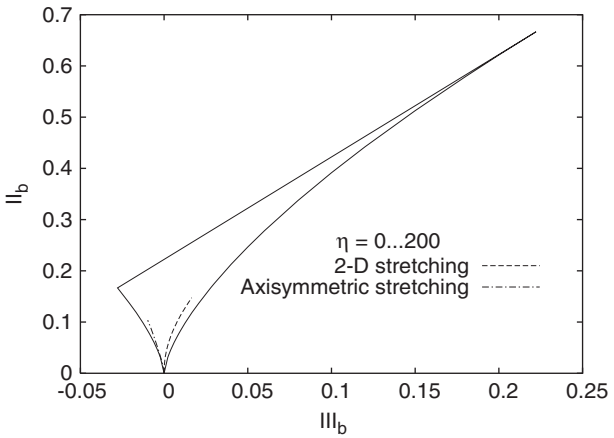

Figure 4. Plane strain phase mapping at different strain rates.

The realizable time scale T_t associated with the present ASM can simply be defined as [24]

$$T_t = \sqrt{\frac{k^2}{\varepsilon^2} + C_T^2 \frac{\nu}{\varepsilon}} = \frac{k}{\varepsilon}\sqrt{1 + \frac{C_T^2}{Re_T}}, \quad Re_T = \frac{k^2}{\nu\varepsilon} \tag{27}$$

where ν denotes the kinematic viscosity and Re_T is the turbulence Reynolds number. Equation (27) warrants that the eddy time scale never falls below the Kolmogorov time scale $C_T\sqrt{\nu/\varepsilon}$, dominant in the immediate neighbourhood of the solid wall. It prevents the singularity in the dissipation equation down to the wall. Alternatively, the turbulence time scale is k/ε at large Re_T but approaches the Kolmogorov limit $C_T\sqrt{\nu/\varepsilon}$ for $Re_T \ll 1$. The empirical constant $C_T = \sqrt{2}$ associated with the Kolmogorov time scale is estimated from the behaviour of k in the viscous sublayer [25]. Articulately, the inclusion of T_t in the ε equation guarantees near-wall asymptotic consistency without resorting to *ad hoc* damping functions employed in many k–ε models [26].

In particular, the eddy viscosity damping function confronts the distinct effects of low-Reynolds number and wall proximity in near-wall regions, and is devised pragmatically as

$$f_\mu = 1 - \exp\left(-\frac{y}{L}\right), \quad L^2 = 2\eta(8 + C_\mu Re_T)\sqrt{\frac{\nu^3}{\varepsilon}} \tag{28}$$

where y is the normal distance from the wall and $(\nu^3/\varepsilon)^{1/4}$ signifies the Kolmogorov length scale. The empirical function f_μ is valid in the whole flow field, including the viscous sublayer and the logarithmic layer. For $C_\mu Re_T > 8$, the present model $C_\mu f_\mu$ seems likely to increase proportionally to y^{-1} in the near-wall region, as evinced by Figure 5 in comparison with the DNS data [27] for a fully developed turbulent channel flow. Alternatively, the adopted form of $C_\mu f_\mu$ converges to replicate the influences of low-Reynolds number and wall proximity. In this figure the abbreviations SSGZ and MCH stand for the models of So *et al.* [9] and modified Chien [10], respectively. The product $C_\mu f_\mu \approx 0.09$ (the standard choice for $C_\mu = 0.09$, pertaining to the k–ε model) remote from the wall to ensure that the model is compatible

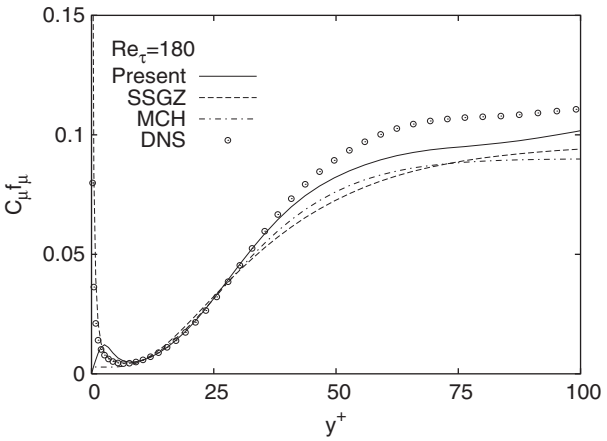

Figure 5. Variations of eddy viscosity coefficients with wall distance in channel flow.

with the standard k–ε turbulence model. The use of $f_\mu = f_\mu(y, L)$ confronts the singularity at neither the separating nor the reattaching point in contrast to the adoption of $y^+ = u_\tau y/\nu$, where u_τ is the friction velocity. Consequently, the model is applicable to separated and reattaching flows. In principle, the construction of $C_\mu f_\mu$ compared with the traditional one [26] reduces the potentiality of $C_\mu f_\mu$ to grow particularly in near-wall regions (i.e. the traditional/conventional formulation gets high magnitudes of $C_\mu f_\mu$ while approaching the wall), as represented faithfully by Figure 5.

Near-wall flows show a tendency to underestimate the dissipation rate ε due to the local anisotropy of turbulence, adhering to the nondimensional parameter P/ε [28, 29]. The formulation has been developed to enhance dissipation in such a situation using the relation: $C_{\varepsilon 1} = C^*_{\varepsilon 1} + a_1 P/\varepsilon$, where $C^*_{\varepsilon 1}$ and a_1 are model constants [30, 31]. However, this procedure can cause numerical instability in more complex flows. One possible approach to counteracting this adverse situation is to explore alternative elements with relevance to P/ε:

$$C_{\varepsilon 1} = 1 + \left(\frac{\beta}{C_T}\right)^2, \quad C_{\varepsilon 2} = C_T \tag{29}$$

where β is evaluated earlier. It can be stressed that the rational subsistence β to P/ε indubitably is conducive to allowing a compatible change in $C_{\varepsilon 1}$ (i.e. $1 \leqslant C_{\varepsilon 1} < 1.1$) which accounts for the additional production of dissipation by the anisotropy of turbulence. Herein, one remarkable departure from the conventional modelling needs to be noted. The coefficient $C_{\varepsilon 2}$ is reduced from its usual value of 1.92 to $C_T = \sqrt{2}$ while $C_{\varepsilon 1}$ is made a function of the invariants. However, $C_{\varepsilon 2}/C_{\varepsilon 1} \approx 1.35$ in the log layer of channel flow, (where $\eta = T_t S = T_t W = 3.3$) converging toward the standard $C_{\varepsilon 2}$-to-$C_{\varepsilon 1}$ ratio ($1.92/1.44 = 1.33$).

The extra source term E_ε in Equation (8) is constructed from the most extensive turbulence diffusion models for k and ε equations derived by Yoshizawa [32] with the two-scale direct-interaction approach using the inertial-range simplification. To receive positive benefits from the numerical reliability and to integrate the inertial-range condition directly to the solid wall,

the cross-diffusion term is designed as [24]

$$E_\varepsilon = C_\varepsilon \frac{\mu_T}{T_t} \max\left[\frac{\partial(k/\varepsilon)}{\partial x_i}\frac{\partial k}{\partial x_i}, 0\right] \tag{30}$$

where $C_\varepsilon = 2$. Obviously, the source term E_ε stimulates the energy dissipation in nonequilibrium flows, thereby reducing the departure of the turbulence length scale from its local equilibrium value and enabling improved prediction of adverse pressure gradient flows accompanied by flow separation and reattachment. At this stage, it appears necessary to identify that the quantity E_ε is characteristically beneficial in the vicinity of the reattachment point and hence, it can be regarded as an attempt at replacing the Yap correction [33]. It is appropriate to stress here that unlike the isotropic model with a constant C_μ, the present anisotropic model having the standard values $C_{\varepsilon(1,2)}$ $(1.44, 1.92)$ and E_ε in the dissipation equation, overestimates the recirculation length of separated flows (for instance, backward facing step and diffuser flows) compared with experimental data. To avoid this situation, the above-mentioned physical adjustments are introduced with $C_{\varepsilon(1,2)}$.

The budgets of k and ε from the DNS data confirm that the role of turbulence diffusion in the near-wall region is substantial. Accordingly, the Prandtl numbers σ_k and σ_ε are modelled, rather than being assigned constant values (unlike the commonly adopted practice with $\sigma_k = 1.0$, and $\sigma_\varepsilon = 1.3$):

$$\sigma_k = C_\mu^{3/4} + f_\mu, \quad \sigma_\varepsilon = \sqrt{C_\mu} + f_\mu \tag{31}$$

The model coefficients σ_k and σ_ε are developed so that sufficient diffusion is obtained in the vicinity of the wall. This contrivance tends to successfully predict the kinetic energy and dissipation rate profiles [34].

The transport equations for k and ε are subjected to the following boundary conditions at solid walls:

$$k_w = 0, \quad \varepsilon_w = 2\nu\left(\frac{\partial\sqrt{k}}{\partial y}\right)^2 \approx 2\nu\frac{k}{y_n^2} \tag{32}$$

To avoid numerical instability, the approximation for ε_w is applied at the first grid node neighbouring the wall, rather than on the wall itself. This requires the normal distance from a wall to the nearest grid point, which is unambiguous and readily available. The validity of Equation (32) necessitates that the grid system is fine enough to produce the near-wall limiting behaviour.

3. COMPUTATIONS

To validate the generality and efficacy of the present model, a few applications to two-dimensional turbulent flows consisting of a fully developed channel flow, a flat plate boundary layer flow with zero pressure gradient, a backward-facing step flow and an asymmetric plane diffuser flow are considered. For a comparison purpose, calculations from the SSGZ and MCH models are included. The possible reasoning for the choice of the isotropic SSGZ and MCH models is that they contain similar types of near-wall correction terms having constant coefficients. Furthermore, they use the Kolmogorov and Taylor scales in the eddy viscosity

damping functions to account for near-wall effects. Therefore, they are supposed to evaluate the combined effects of low-Reynolds number and near-wall turbulence with reasonable accuracy. However, compared with the SSGZ and MCH models, the new nonlinear model is additionally sensitized to nonequilibrium and anisotropic effects.

A cell-centred finite-volume scheme together with an artificial compressibility approach [35] is employed to solve the flow equations. In the artificial compressibility method, the artificial compressibility is principally added to the derivative of density with respect to the pressure, influencing not only the continuity equation but also the other equations. The energy equation is not decoupled from the system of equations, which facilitates a uniform treatment for both the primitive and conservative variables. A fully upwinded second-order spatial differencing is applied to approximate the convective terms. Roe's damping term [36] is used to calculate the flux on the cell face. A diagonally dominant alternating direction implicit (DDADI) time integration method [37] is applied for the iterative solution of the discretized equations. A multigrid method is utilized for the acceleration of convergence [38]. The basic implementation of the artificial compressibility method and associated features are described in References [35, 39].

A variable grid spacing is used to resolve the sharp gradient in near-wall regions. Grid densities are varied to ensure the grid independence of the numerical results. It is found that the solution is not very sensitive to the number of grid points as long as there are two points in $y^+ < 1.5$. In the computations that follow, convergence is judged by monitoring the root-mean-square residuals of mass and momentum. The solution is taken as having converged when all residuals are of the order 10^{-4} or less. To this end, it must be emphasized that comparing with the present nonlinear model, the isotropic turbulence models (i.e. SSGZ and MCH) converse to a lower state for the same number of iteration cycles. In principle, the additional correction terms in the Reynolds stress expression of the anisotropic model are dispersive rather than dissipative, a feature that slows down the convergence.

3.1. *Channel flow*

Computations are carried out for a fully developed turbulent channel flow at $Re_\tau = 180$, for which turbulence quantities are attainable from the DNS data [27]. Calculations are conducted in the half-width of the channel, imposing periodic boundary conditions, except for the pressure, pertaining to the upstream and downstream boundaries. A 48×48 nonuniform grid refinement is considered to be sufficiently accurate to describe the flow characteristics. For this case, the length of the computational domain is 32δ, where δ is the channel half-width. To ensure the resolution of the viscous sublayer, the first grid node near the wall is placed at $y^+ \approx 0.4$. Comparisons are made by plotting the results in the form of $u^+ = u/u_\tau$, $k^+ = k^+/u_\tau^2$, $uv^+ = \overline{uv}/u_\tau^2$, $\varepsilon^+ = \nu\varepsilon/u_\tau^4$, $uu^+ = \sqrt{\overline{uu}}/u_\tau$, $vv^+ = \sqrt{\overline{vv}}/u_\tau$ and $ww^+ = \sqrt{\overline{ww}}/u_\tau$ versus y^+. To compute the $\overline{ww}$ component for this two-dimensional flow, the usual approximation $\overline{ww} = 2k - \overline{uu} - \overline{vv}$ is employed.

Figure 6 shows the profiles of mean velocity, shear stress, turbulent kinetic energy and dissipation rate for different models. As is evident, predictions of the present, SSGZ and MCH models agree well with the DNS data. However, the MCH model predicts a peak of ε^+ at a slightly shifted location. In strong contrast, the present and SSGZ models provide a maximum ε^+ at the wall which is more in line with the experimental and DNS data.

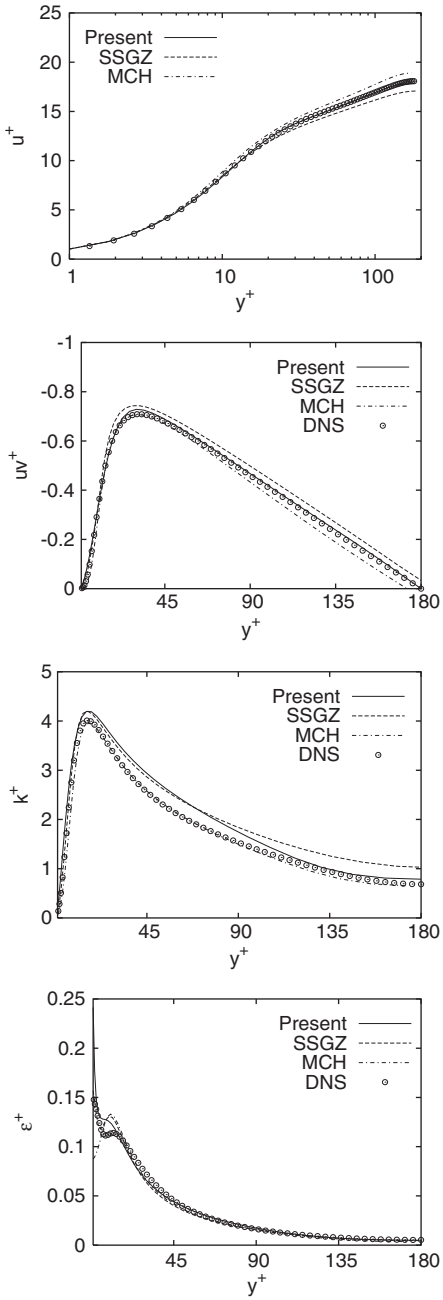

Figure 6. Channel flow predictions compared with DNS results at $Re_\tau = 180$.

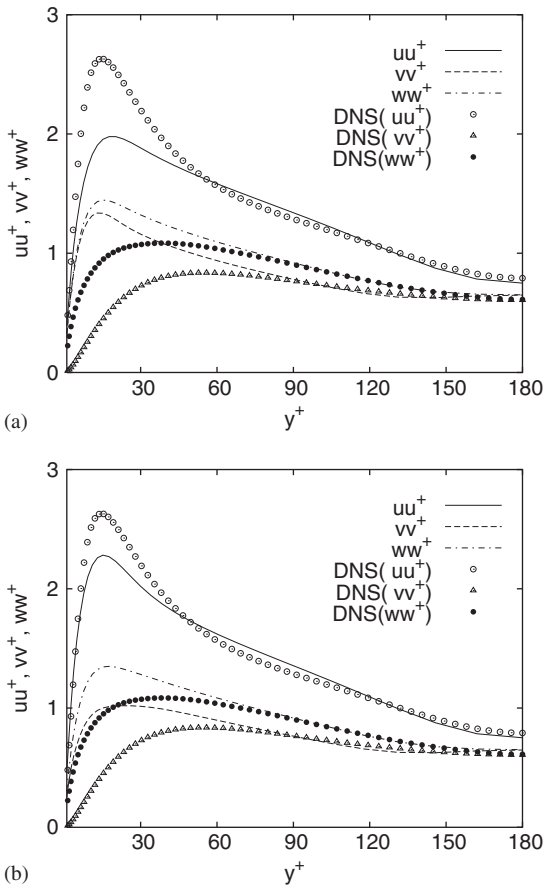

Figure 7. Normal stress profiles in channel flow at $Re_\tau = 180$.

Profiles of the turbulent normal stress components are compared with the DNS data in Figure 7. In the present model investigated herein, the influence of the damping function f_μ is an important factor in predicting the energy components for the channel flow. Figure 7(a) shows that relative to the DNS data, the energy component uu^+ is underpredicted and vv^+/ww^+ is overestimated in the region confined to $0 < y^+ < 60$. As f_μ is removed from the nonlinear terms on the right-hand side in Equation (9), the present model provides the closest agreement with the DNS data, shown in Figure 7(b). Note that no appreciable changes are found in other (i.e. u^+, uv^+, k^+ and ε^+) profiles in this case. Nevertheless, this is an unconventional practice and therefore, remains unattempted hereinafter.

3.2. *Flat plate boundary layer flow*

The performance of the proposed model is further contrasted with the experimental data of the flow over a flat plate with a high free stream turbulence intensity. The test case is taken from 'ERCOFTAC' Fluid Dynamics Database [40]. Measurements down to $x = 1.495$ m

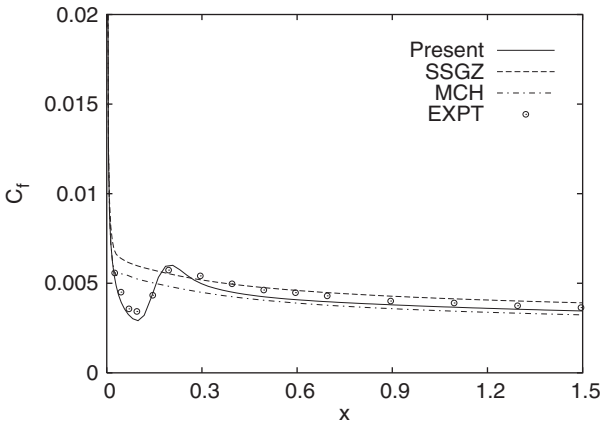

Figure 8. Streamwise skin friction coefficient of boundary layer flow.

which corresponds to $Re_x \approx 94\,000$, are made by Coupland at Rolls-Royce. The inlet velocity is 9.4 m/s and the pressure gradient is zero. The upstream turbulence intensity $T_u = 6.0\%$, defined as $T_u = \sqrt{\frac{2}{3}k}/U_{\text{ref}}$, where U_{ref} indicates the reference velocity. The dissipation is set so that the decay of free stream turbulence is in balance [41].

Computations begin 16 cm ahead of the leading edge and symmetric conditions are applied. The length and height of the grid are 1.6 and 0.3 m, respectively. The near-wall grid node is located at $y^+ < 1.0$, except the point at the leading edge ($y^+ = 2.1$). The grid size is 96×64 and heavily clustered near the wall.

The predicted skin friction coefficients ($C_f = 2u_\tau^2/U_{\text{ref}}^2$) are compared with the experimental data in Figure 8. Both the SSGZ and MCH models, having the wall distance in the damping functions provide earlier transition than that seen in the experiment, coincident with Savill's investigation [42]. Although the present model uses the wall-distance to characterize near-wall viscous effects on turbulence, returns the best skin friction in terms of its magnitude and trend. The physical reasoning is that the nonlinear eddy viscosity model resolves normal stress anisotropy and returns a substantially different response of turbulence to rotational and irrotational straining, in accord with reality [41]. Seemingly, the agreement of all models with the experiment is fairly good toward the end of the transition (e.g. beyond $x = 0.195$ m).

3.3. *Backward-facing step flow*

To ascertain the performance in complex separated and reattaching turbulent flows, the present model is applied to the flow over a backward-facing step. The computations are conducted corresponding to the experimental case with zero deflection of the wall opposite to the step, as investigated by Driver and Seegmiller [43]. The reference velocity $U_{\text{ref}} = 44.2$ m/s and the step height $h = 0.0127$ m. The ratio between the channel height and the step height is 9, and the step height Reynolds number is $Re = 3.75 \times 10^4$. At the channel inlet, the Reynolds number based on the momentum thickness is $Re_\theta = 5.0 \times 10^4$.

For the computations, grids are arranged in two blocks. The smaller one (extended from the inlet to the step) contains a 16×48 nonuniform grid and the grid size for other one

is 120×80. The maximum height of the first near-wall grid node is at $y^+ < 1.5$. The inlet conditions are specified four step heights upstream of the step corner and the outlet boundary conditions are imposed 30 step heights downstream of the step corner. The inlet profiles for all dependent variables are generated by solving the models at the appropriate momentum thickness Reynolds number. All the quantities shown below are normalized by the step height h and the experimental reference free stream velocity U_{ref}, provided that the distance x/h is measured exactly from the step corner.

Computed and experimental friction coefficients C_f along the step side wall are plotted in Figure 9. As is observed, all models are in good agreement with the data. However, the SSGZ model exhibits nonphysical trend in the C_f profile near the corner at the base of the step. This is probably due to the improper behaviour of the viscous damping functions employed. The positive C_f that starts from $x/h = 0$ is due to a secondary eddy which sits in the corner at the

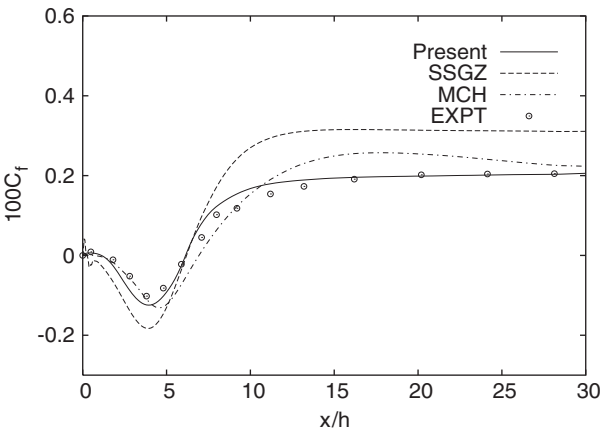

Figure 9. Skin friction coefficient along the bottom wall of step flow.

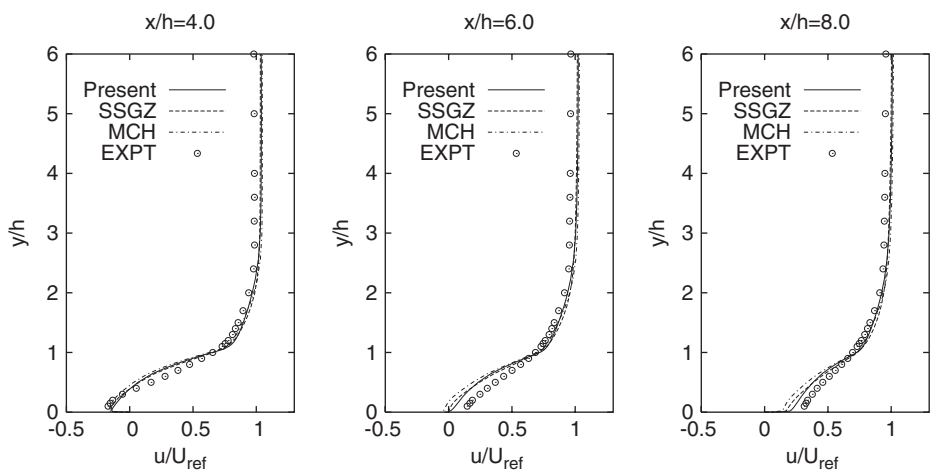

Figure 10. Mean velocity profiles at selected locations for step flow.

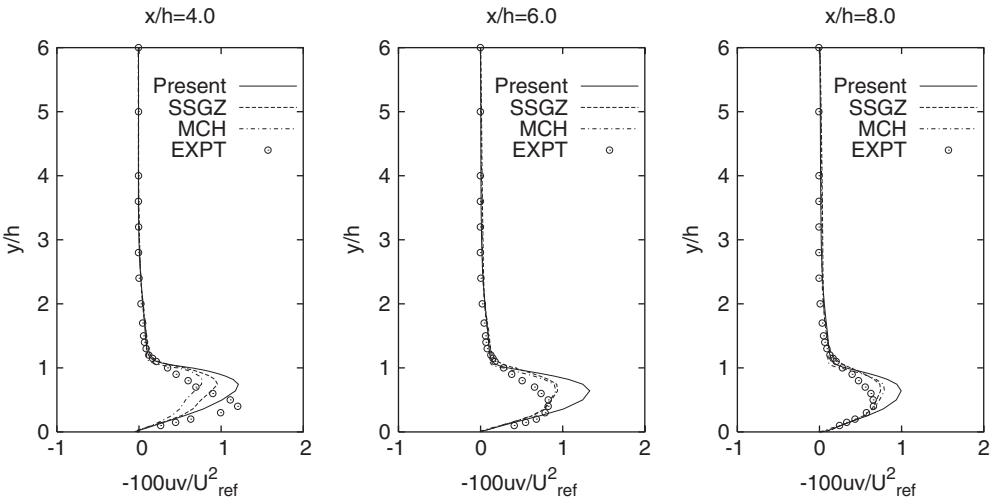

Figure 11. Shear stress profiles at selected locations for step flow.

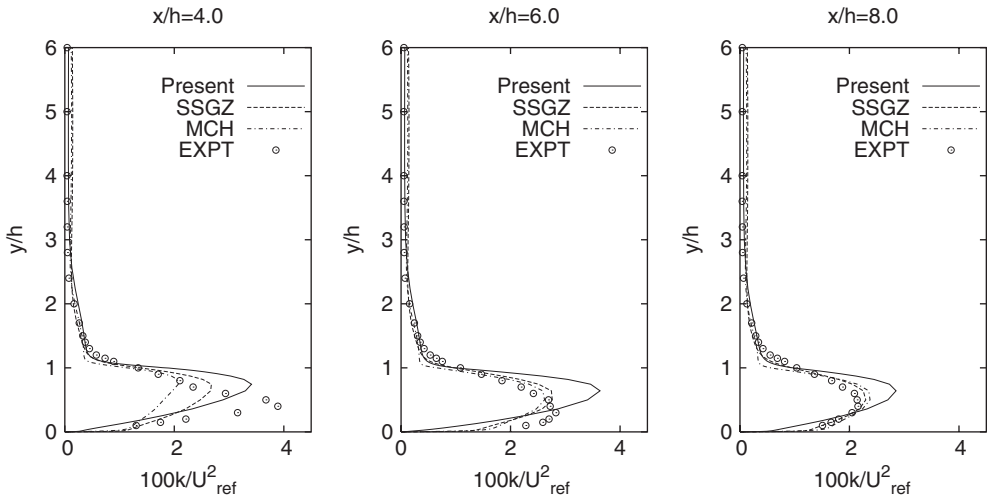

Figure 12. Kinetic energy profiles at selected locations for step flow.

base of the step, inside the main recirculation region. The recirculation lengths predicted by the present, SSGZ and MCH models are $6.1h$, $6.1h$ and $6.8h$, respectively. The experimental value of the reattachment length is 6.26 ± 0.1, making a fairly good correspondence with all models.

The streamwise mean velocity profiles at three representative positions are depicted in Figure 10. Obviously, the predictions of all models are in good agreement with the experiment. Comparisons are extended to the distributions of Reynolds shear stress and the

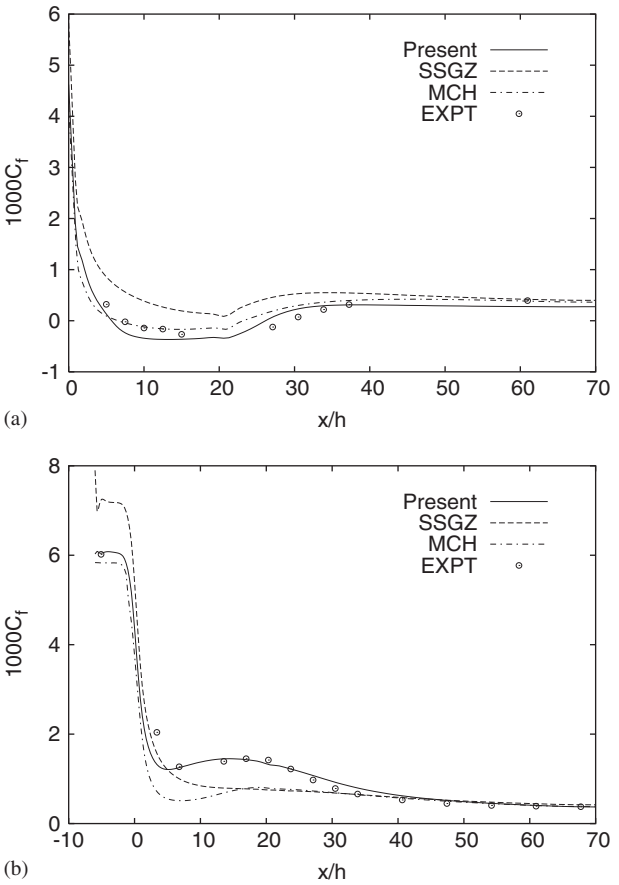

Figure 13. Skin friction coefficients of diffuser flow: (a) along the deflected bottom wall; and (b) along the straight top wall.

corresponding turbulent kinetic energy at different x/h locations behind the step corner, as shown in Figures 11 and 12. A closer inspection of the distribution indicates that all model predictions have satisfactory agreement with the experimental data in both the recirculation and recovery regions.

3.4. Asymmetric plane diffuser flow

To further evaluate the performance, the model is applied to simulate the flow in a plane asymmetric diffuser with an opening angle of 10°, for which measurements are available [44]. The expansion ratio of 4.7 is sufficient to produce a separation bubble on the deflected wall. Hence the configuration provides a test case for smooth, adverse pressure-driven separation. The entrance to the diffuser consists of a plane channel to invoke fully developed flow with $Re = 2.0 \times 10^4$ based on the centerline velocity U_{ref} and the inlet channel height h. Computations involving a 120×72 nonuniform grid resolution are considered to be

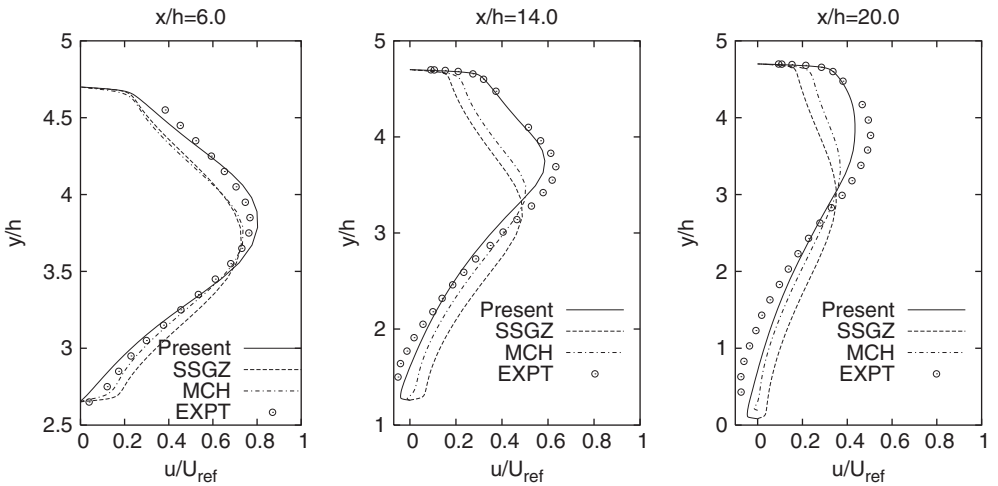

Figure 14. Mean velocity profiles at selected locations for diffuser flow.

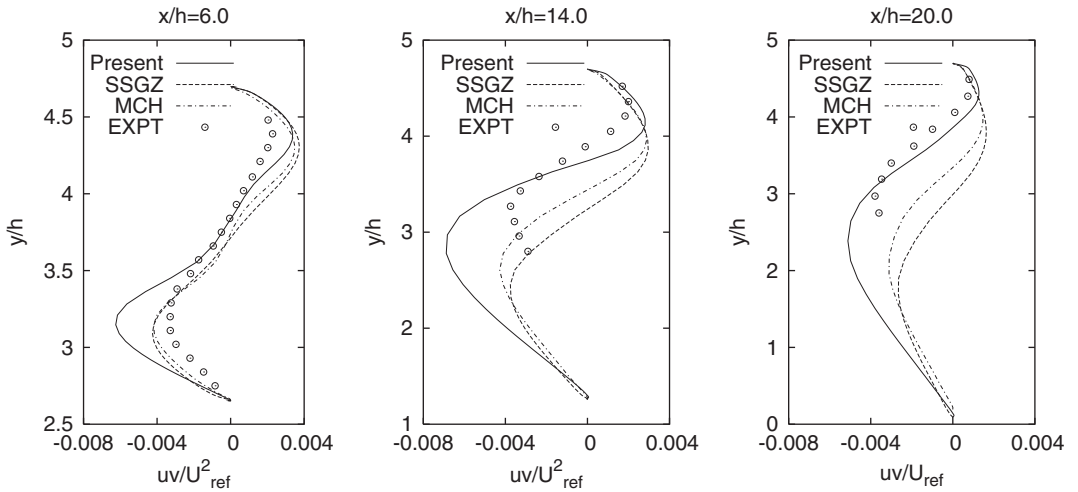

Figure 15. Shear stress profiles at selected locations for diffuser flow.

accurate to describe the flow characteristics. The length of the computational domain is $76h$. The thickness of the first cell remains below one in y^+ units on both the deflected and flat walls.

Figures 13(a) and (b) portray the predicted skin friction coefficients C_f. The performance of both the present and MCH models evinces an encouraging qualitative agreement with measurements. Apparently, the ambiguous prediction regarding the SSGZ model demands a higher value for the proposed correction in the ε equation to render the model results compatible with the experiment. It seems likely that the SSGZ model shows no separation.

Figure 14 exhibits the mean velocity profiles at three representative positions. The overall performance in predicting the velocity profiles is the best for the present model. Toward downstream of the diffuser the computed values of mean velocities, pertaining to both the SSGZ and MCH models become noticeably smaller than the data shown, except near the wall. In principle, the flow associated with the separation bubble is characterized by strongly anisotropic turbulence. The inaccurately predicted velocity fields of the linear variants are attributable to their inability in appropriately responding to strong anisotropy.

Profiles of the shear stress at three representative streamwise positions are given in Figure 15. As is observed, the present model predictions are in broad accord with the measured data. The superiority of the proposed model over the linear variants is once more ascertained. The comparisons of predicted and measured turbulent normal stresses are

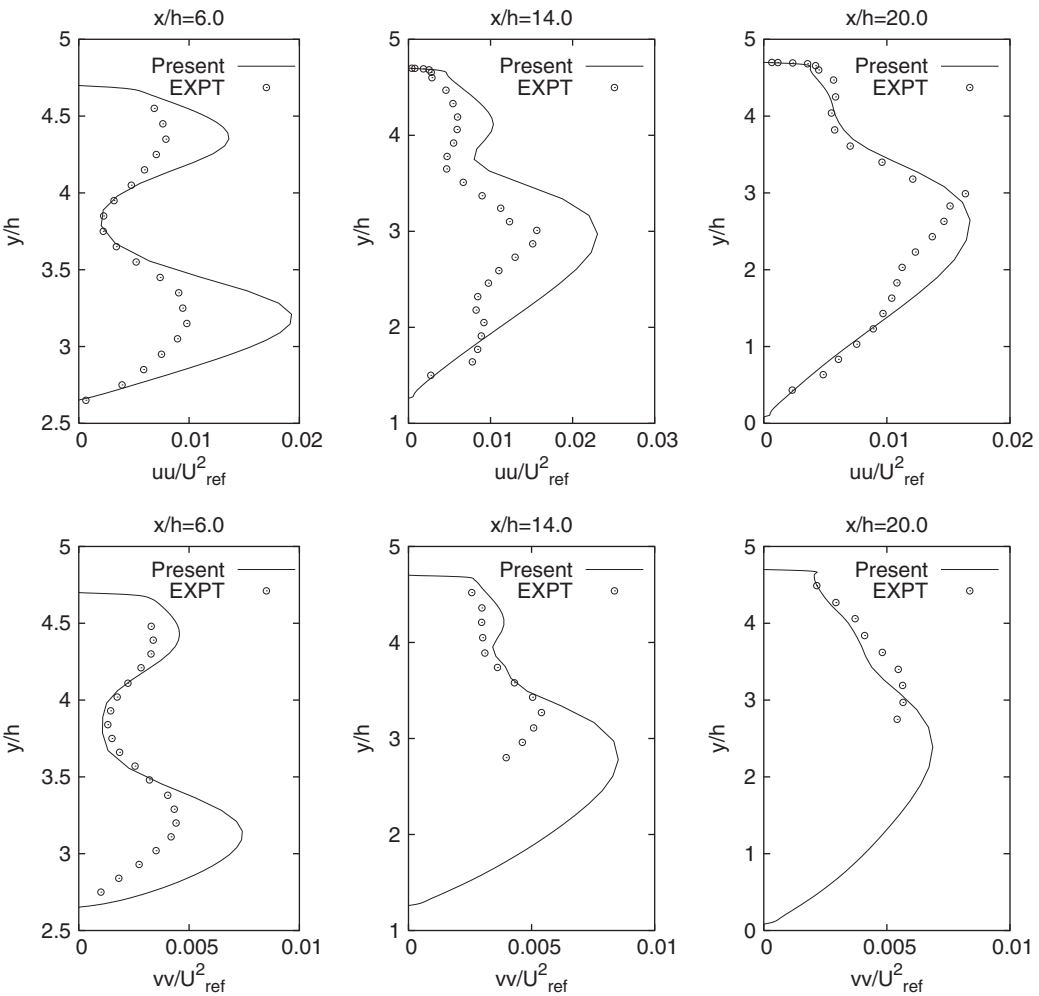

Figure 16. Normal stress profiles at selected locations for diffuser flow.

displayed in Figure 16 at various x/h locations. No results arising from the linear models have been included here as these models are obviously unable to predict realistic levels of normal stress anisotropy. As seen, the present model replicates pronounced turbulence anisotropy for $\overline{uu}$ and $\overline{vv}$, in line with the experimental data.

4. CONCLUSIONS

The present model accounts for the near-wall and low-Reynolds number effects originating from the physical requirements. The model coefficient $C_{\varepsilon 1}$ which is sensitized to both the mean strain rate and rotation rate fields, and a secondary positive source term in the dissipation equation enhance dissipation in near-wall regions. It enforces the realizability constrains as confirmed by the anisotropy invariant map and invokes a simple wall-boundary condition for ε. Contrasting the predicted results with the experimental data for well-documented flows, consisting of a fully developed channel flow, a flat plate boundary layer flow with zero pressure gradient, a backward facing step flow and an asymmetric diffuser flow demonstrates that the new model is capable of reproducing the skin friction coefficients and turbulent quantities with reasonable accuracy. The comparisons approve that the present ASM provides significant improvement over the linear variants of k–ε eddy viscosity models and has good potential to be a practical tool in engineering applications.

REFERENCES

1. Rodi W. A new algebraic relation for calculating the Reynolds stresses. *Zeitschrift fur Angewanate Mathematik und Mechanik* 1976; **56**:T219–T221.
2. Pope SB. A more general effective viscosity hypothesis. *Journal of Fluid Mechanics* 1975; **72**:331–340.
3. Gatski TB, Speziale CG. On the explicit algebraic stress models for complex turbulent flow. *Journal of Fluid Mechanics* 1993; **254**:59–78.
4. Lumley JL. Computational modelling of turbulent flows. *Advances in Applied Mechanics* 1978; **18**:124–176.
5. Abid R, Rumsey C, Gatski TB. Prediction of nonequilibrium turbulent flows with explicit algebraic stress models. *AIAA Journal* 1995; **33**:2026–2031.
6. Girimaji SS. Fully explicit and self-consistent algebraic Reynolds stress model. *Theoretical and Computational Fluid Dynamics* 1996; **8**:387–402.
7. Rumsey CL, Gatski TB, Morrison JH. Turbulence model predictions of strongly curved flow in a U-duct. *AIAA Journal* 2000; **38**:1394–1402.
8. Girimaji SS. A Galilean invariant explicit algebraic Reynolds stress model for turbulent curved flows. *Physics of Fluids* 1997; **9**:1067–1077.
9. So RMC, Sarkar A, Gerodimos G, Zhang J. A dissipation rate equation for low-Reynolds number and near-wall turbulence. *Theoretical and Computational Fluid Dynamics* 1997; **9**:47–63.
10. Rahman MM, Siikonen T. Improved low-Reynolds-number k–$\tilde{\varepsilon}$ model. *AIAA Journal* 2000; **38**:1298–1300.
11. Jones WP, Launder BE. The calculation of low-Reynolds number phenomena with a two-equation model of turbulence. *International Journal of Heat and Mass Transfer* 1973; **16**:1119–1130.
12. Craft TJ, Launder BE, Suga K. Extending the applicability of eddy-viscosity model through the use of deformation invariant and non-linear elements. *Proceedings of the Fifth International Symposium on Refined Flow Modelling and Turbulence Measurements* 1993; 125.
13. Craft TJ, Launder BE, Suga K. Development and application of a cubic eddy viscosity model of turbulence. *International Journal of Heat and Fluid Flow* 1996; **17**:108–115.
14. Rung T, Thiele F, Fu S. On the realizability of nonlinear stress–strain relationships for Reynolds stress closures. *Flow, Turbulence and Combustion* 1999; **60**:333–359.
15. Shih T-H, Zhu J, Lumley JL. A new Reynolds stress algebraic equation model. *Computer Methods in Applied Mechanics and Engineering* 1995; **125**:287–302.
16. Jongen T, Gatski TB. A new approach to characterizing the equilibrium states of the Reynolds stress anisotropy in homogeneous turbulence. *Theoretical and Computational Fluid Dynamics* 1998; **11**:31–47.
17. Kim J. Personal communication, 1990.

18. Tavoularis S, Corrsin A. Experiments in nearly homogeneous turbulent shear flow with a uniform mean temperature gradient. *Journal of Fluid Mechanics—Part I* 1981; **104**:311–347.
19. Abid R, Speziale CG. Predicting equilibrium states with Reynolds stress closures in channel flow and homogeneous shear flow. *Physics of Fluids A* 1997; **5**:1776–1782.
20. Kim J, Moin P, Moser R. Turbulence statistics in fully developed channel flow at low Reynolds number. *Journal of Fluid Mechanics* 1987; **177**:133–166.
21. Lee MJ, Kim J, Moin P. Structure of turbulence at high shear rate. *Journal of Fluid Mechanics* 1990; **216**:561–583.
22. Rogers MM, Moin P. The structure of the vorticity field in homogeneous turbulent flows. *Journal of Fluid Mechanics* 1987; **176**:33–66.
23. Cazalbou JB, Bradshaw P. Turbulent transport in wall bounded flows. Evaluation of model coefficients using direct numerical simulation. *Physics of Fluids* 1993; **5**:3233–3239.
24. Rahman MM, Siikonen T. Near-wall turbulence modelling with enhanced dissipation. *International Journal for Numerical Methods in Fluids* 2003; **42**:979–997.
25. Rahman MM, Rautaheimo P, Siikonen T. Modifications for an explicit algebraic stress model. *International Journal for Numerical Methods in Fluids* 2001; **35**:221–245.
26. Patel VC, Rodi W, Scheuerer G. Turbulence models for near-wall and low Reynolds number flow: a review. *AIAA Journal* 1985; **23**:1308–1319.
27. Mansour NN, Kim J, Moin P. Reynolds-stress and dissipation-rate budgets in a turbulent channel flow. *Journal of Fluid Mechanics* 1988; **194**:15–44.
28. Mansour NN, Kim J, Moin P. Near-wall k–ε turbulence modelling. *AIAA Journal* 1989; **27**:1068–1073.
29. Durbin PA, Speziale CG. Local anisotropy in strained at high Reynolds numbers. *Journal of Fluids Engineering* 1991; **113**:707–709.
30. Durbin PA. A Reynolds-stress model for near-wall turbulence. *Journal of Fluid Mechanics* 1993; **249**:465–498.
31. Ahn JW, Park TS, Sung HJ. Application of a near-wall turbulence model to the flows over a step with inclined wall. *International Journal of Heat and Fluid Flow* 1997; **18**:209–217.
32. Yoshizawa A. Statistical modelling of a transport equation for the kinetic energy dissipation rate. *Physics of Fluids A* 1987; **30**:628–631.
33. Yap CR. Turbulent heat and momentum transfer in recirculating and impinging flows. *Ph.D. Thesis*, Faculty of Technology, University of Manchester, 1987.
34. Abe K, Kondoh T, Nagano Y. On Reynolds-stress expressions and near-wall scaling parameters for predicting wall and homogeneous turbulent shear flows. *International Journal of Heat and Fluid Flow* 1997; **18**:266–282.
35. Rahman MM, Rautaheimo P, Siikonen T. Numerical study of turbulent heat transfer from a confined impinging jet using a pseudo-compressibility method. In *Second International Symposium on Turbulence, Heat and Mass Transfer*, Delft, The Netherlands, 1997; 511–520.
36. Roe PL. Approximate Riemann solvers, parameter vectors, and difference schemes. *Journal of Computational Physics* 1981; **43**:357–372.
37. Lombard C, Bardina J, Venkatapathy E, Oliger J. Multi-dimensional formulation of CSCM—an upwind flux difference eigenvector split method for the compressible Navier–Stokes equations. In *Sixth AIAA Computational Fluid Dynamics Conference*, AIAA Paper 83-1895-CP, 1983; 649–664.
38. Jameson A, Yoon S. Multigrid solution of the Euler equations using implicit schemes. *AIAA Journal* 1986; **24**:1737–1743.
39. Rahman MM, Siikonen T. An artificial compressibility method for incompressible flows. *Numerical Heat Transfer, Part B* 2001; **40**:391–409.
40. Coupland J. Flat plate transitional boundary layers. *ERCOFTAC Fluid Dynamics Database* (*http://ercoftac.mech.surrey.ac.uk/*), 1990.
41. Chen WL, Lien FS, Leschziner MA. Nonlinear eddy viscosity modelling of transitional boundary layers pertinent to turbomachine aerodynamics. *International Journal of Heat and Fluid Flow* 1998; **19**:297–306.
42. Savill AM. Some recent progress in the turbulence modelling of by-pass transition. In *Near-Wall Turbulent Flows*, So RMC, Speziale CG, Launder BE (eds). Elsevier: Amsterdam, 1993; 829–848.
43. Driver DM, Seegmiller HL. Features of a reattaching turbulent shear layer in divergent channel flow. *AIAA Journal* 1985; **23**:163–171.
44. Buice C, Eaton JK. Experimental investigation of flow through an asymmetric plane diffuser. *Report TSD-107*, Department of Mechanical Engineering, Thermoscience Division, Stanford University, California, CA, 1997.

